Meteorology and Atmospheric Physics (2026) 138:82
https://doi.org/10.1007/s00703-026-01186-z

RESEARCH

Analysis of a large-hail producing supercell and its merger with a nascent supercell on 6 october 2015

Maurício I. Oliveira[1,2] · **Vitor Goede**[3] · **Eliton L. Figueiredo**[4] · **Murilo M. Lopes**[2] · **Rafael J. C. Santana**[2] · **Ernani L. Nascimento**[5] · **Ming Xue**[6] · **Lucas I. G. Oliveira**[2] · **Franciano S. Puhales**[2] · **Vanessa Ferreira**[7]

Received: 1 March 2026 / Accepted: 29 July 2026

Abstract

This study documents the lifecycle and large-scale environment of a large-hail producing supercell that occurred in southern Brazil (SB) on 6 October 2015. The supercell underwent a merger with a nascent supercell near a Doppler weather radar and rapidly intensified shortly after the interaction. The original (premerger) supercell developed in a high-shear, high-instability pre-cyclogenesis environment and remained isolated until the merger due to the presence of a relatively rare elevated mixed layer that helped suppress widespread convection and provided steep lapse rates for robust updrafts. A small cell developed ~ 30 km to the north of the original supercell and merged in between its inflow and forward-flank regions, resulting in a new (postmerger) supercell that inherited the main features of the intensifying nascent cell. Radar-derived quantities related to supercell intensity reveal that the updraft and mesocyclone intensified significantly within 30 min of the merger, resulting in a large episode of hailfall with 6 + cm hail reported at the surface. After reaching peak intensity, the postmerger supercell and its attendant low-level mesocyclone rapidly decayed, likely as a result of a hailfall-induced outflow surge and large convective inhibition. This case illustrates the importance of mergers between mature and nascent supercells to the short-term forecasting of severe weather, a topic that received little attention in studies and prediction of storms in SB.

1 Introduction

Supercell storms occur frequently in southern Brazil (SB) (Fig. 1a), where they often produce tornadoes (Oliveira et al. 2022; Ferreira et al. 2022; Salio et al. 2024; Schild et al. 2024; Lopes et al. 2025), large hail, and damaging wind gusts (Bechis et al. 2025). Despite their frequency and high impact, supercells in SB have rarely been studied, mainly due to the sparse Doppler radar coverage until recent years, which often failed to capture significant events less than 100 km from the nearest radar. The distant sampling issue is aggravated by the limited quality of the radar variables and the lack of standardized scanning strategies aimed at sampling convective storms. The latter issue stems from the widespread use of scanning strategies based on staggered pulse repetition times (PRTs), which can extend the Nyquist intervals and reduce the occurrence of velocity aliasing during velocity estimates (Zrinc and Mahapatra 1985), but also produce a high number of erroneously estimated radial velocities if the ratio between the short and long PRTs is close to unity (Sachidananda and Zrinc 2000, 2002; Torres et al. 2004). Even with the development of more advanced

✉ Maurício I. Oliveira
mauricio.meteorologia@gmail.com

1 Instituto Nacional de Pesquisas da Amazônia, Manaus, Amazonas, Brazil

2 Grupo de Modelagem Atmosférica, Departamento de Física, Universidade Federal de Santa Maria, Santa Maria, Rio Grande do Sul, Brazil

3 Advanced Radar Research Center, School of Meteorology, University of Oklahoma, Norman, OK, USA

4 Centro de Pesquisas e Previsões Meteorológicas, Universidade Federal de Pelotas, Pelotas, Rio Grande do Sul, Brazil

5 Meteorological Satellites and Sensors Division, National Institute for Space Research, Cachoeira Paulista, São Paulo, Brazil

6 Center for Analysis and Prediction of Storms, School of Meteorology, University of Oklahoma, Norman, OK, USA

7 Land Surface-Atmosphere Interaction, Technical University of Munich (TUM), Munich, Germany

Published online: 12 August 2026

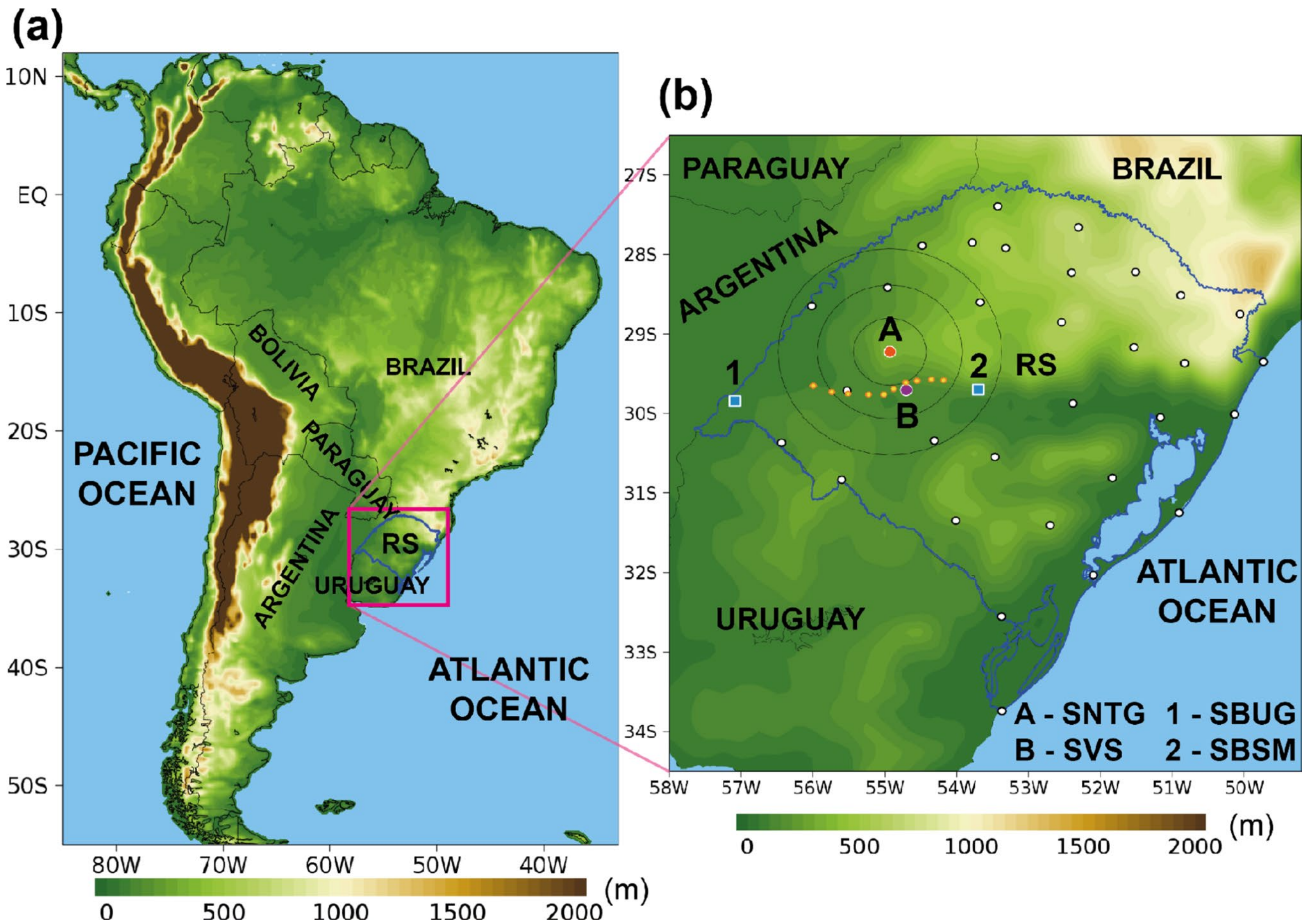

Fig. 1 (**a**) Terrain elevation map of South America. The thin black and thick blue contours outline country borders and the Rio Grande do Sul (RS) state, respectively. The magenta box encompasses a zoomed-in view of RS in (**b**). (**b**) RS and neighboring countries. Small white circles denote the spatial distribution of INMET surface stations in RS. Red and purple circles A and B indicate, respectively, the locations of the Santiago (SNTG) radar and São Vicente do Sul (SVS). The concentric lines around A denote the radar range circles at 50 km intervals. The blue squares 1 and 2 represent the Uruguaiana (SBUG) and Santa Maria (SBSM) sounding sites, respectively. In both (**a**) and (**b**), color shading represents terrain elevation. The track of the SVS supercell's centroid is denoted by the yellow circles in (**b**)

correction techniques (Alford et al. 2022), this makes the detection of mesocyclones—the defining characteristic of supercells—complicated in an operational setting (Goede 2022). The identification of supercells either in operational or research settings often has to rely on alternative features associated with supercellular convection, such as persistent deviant motion (Bunkers et al. 2000, 2022) to the left of the deep-layer shear vector (for clockwise, cyclonically rotating storms in the Southern Hemisphere; Nascimento et al. 2014), cell splittings (Rotunno and Klemp 1985), storm longevity (Bunkers et al. 2006a, b), reflectivity echo features such as bounded-weak echoes/weak echo regions (BWERs/WERs; Chisholm 1973), hook echoes (Lemon and Doswell 1979), and visual observations of supercell-related phenomena (Ribeiro et al. 2022).

The aforementioned scarcity of close-range radar observations of supercells and the data quality limitations have resulted in incomplete understanding of supercell evolution in SB. For instance, the short-term evolution of convective storms, including supercells, can be rather sensitive to their mergers with nearby cells (e.g., Simpson et al. 1980; Westcott 1984, 1994) and the environment in which the mergers occur (Wurman et al. 2007; Flournoy et al. 2022; Lyza and Flournoy 2023; Nixon et al. 2024). Using an idealized numerical framework, Hastings and Richardson (2016) simulated several scenarios of mergers between mature and nascent supercells by varying the time and location of initiation of the nascent storms while keeping the background environment fixed to determine the impact of mergers on the intensity and structure of postmerger storms. The authors identified five different types of mergers that may occur depending on the minimal distance between the mature supercell updrafts to the nascent cells and the relative maturity of the nascent cells. The types of merger include (a) forward-flank mergers, where strong cold pools from nascent cells cut off the inflow of and dissipate the original supercell, causing the nascent storm to become dominant, (b) forward-flank mergers resulting in a multicore system, which subsequently evolves in a dominant supercell, (c) updraft collisions between the original supercell and nascent cells intermediated by a cloud bridging (Simpson et al. 1980; Westcott 1984, 1994), leading to the dissipation of original cell and intensification of the nascent storm into a classic supercell, (d) forward-flank mergers with a cold pool surge resulting in a bow echo, and (e) rear-flank mergers with a cold-pool surge resulting in a high-precipitation (HP) supercell or bow echo depending on the maturity of the nascent cell. The variety of merger possibilities and their outcomes can have a significant impact on the ensuing convective hazards, with some types of constructive mergers favoring large hail (e.g., Piasecki et al. 2023) and others favoring tornadoes (Lee et al. 2006; Wurman et al. 2007; Lyza and Flournoy 2023; Fischer et al. 2023; Nixon et al. 2024).

This study analyzes the life cycle as well as the synoptic- and mesoscale environments of a cyclonic (left-moving) supercell and its merger with a nascent supercell on 6 October 2015 in west-central Rio Grande do Sul (RS) in SB (Fig. 1b). This event is particularly noteworthy due to its proximity to a Doppler radar located in northwestern RS, allowing sufficiently high-resolution observations during the storm merger near the city of São Vicente do Sul (SVS). Following the merger, the resulting supercell immediately intensified, producing large hail and several radar-observed signatures related to severe weather phenomena, including multiple hook echoes, rear-flank gust fronts (RFGFs), BWERs, in addition to a lightning jump. In addition, this study discusses the potential role played by an elevated mixed layer (EML), a feature that has received limited attention in SB (Ribeiro and Bosart 2018), in establishing an environment supportive of isolated to semi-discrete supercell formation. Despite the intrinsic limitations of a case study, this work is an important piece of a larger efforts to improve the documentation and understanding of severe storms in SB (Ribeiro et al. 2022). Collectively, the result of such efforts can highlight avenues for improving the forecasting of convective hazards in SB.

The remainder of this article is organized as follows. Section 2 describes the meteorological datasets. Section 3 evaluates the synoptic- and mesoscale setups conducive to the supercell event and provides an in-depth radar-based analysis of supercell merger process, the resulting storm behavior, and associated radar signatures. The main findings, implications for forecasting, and conclusions are offered in Sect. 4.

2 Data and methods

2.1 Doppler radar data

The analysis of the storms employed data from the Santiago (SNTG) Doppler weather radar (29.23°S–54.93°W; elevation: 434 m; see Fig. 1b), as the storms remained within 60 km southwest to southeast of the radar site throughout most of its life cycle. STNG is operated by the Department of Airspace Control of the Brazilian Air Force (DECEA; in Portuguese) at S-band using the standard transmission and reception of horizontally polarized waves, generating the default Doppler spectral moments: horizontal reflectivity factor (Z_H), radial velocity (v_r), and spectrum width. Its standard scanning strategy consists of a full set of 15 plan-position indicators (PPIs), starting at a 0.5° elevation angle and ending at 18°, taking 5 min to complete a full volume. This is followed by three additional PPIs in extended range surveillance mode (not analyzed in this study), resulting in a full volume update time of 10 min. The radar's range resolution is 500 m, and its nominal 3-dB beamwidth is 1.98°, but oversampling in azimuth yields an effective resolution of 1.15°.

The staggered PRT employed a ratio of 3:4 between the short and long PRTs and resulted in 33 samples per radial, while yielding an unambiguous range r_a = 250 km and an unambiguous velocity v_a = 49.05 m s^{-1}. As previously mentioned, one of the main challenges in the radar dataset was the presence of unfolding errors resulting from the statistical uncertainties arising from the coupled phase noise during the retrieval of the real v_r. Areas of range gates of wrongly dealiased v_r tended to concentrate around important storm features such as the mesocyclone and areas of increased convergence (gust fronts), where increased statistical fluctuations in the phase estimates are expected (Torres et al. 2004). The correction of these wrongfully dealiased range gates was conducted using the methodology proposed in Alford et al. (2022), which can accurately correct a large fraction of these errors (Lopes et al. 2025). However, areas of strong turbulence and perceived low signal quality were inadvertently censored by the radar's processor, leaving small regions of missing v_r that could not be recovered in the absence of the raw In-phase/Quadrature time series.

The retrieval of additional single-polarization variables was carried out using a series of well-established methodologies. The vertically integrated liquid (VIL) was obtained for every volume by vertically integrating columns of Z_H centered in every range gate starting at the lowest elevation, as in Amburn and Wolf (1997). Storm echo tops (ETs) were obtained using the interpolation method developed by Lakshmanan et al. (2013), based on a constant Z_H threshold. The VIL density (VILD) was obtained by dividing the vertically integrated liquid (VIL) and the 18-dBZ ETs (Amburn and Wolf 1997; Murillo and Homeyer 2019). Additional hail variables derived from Z_H include the probability of severe hail (POSH) and maximum expected size of hail (MESH) variables developed by Witt et al. (1998), and later improved by Murillo and Homeyer (2019).

To determine mesocyclone intensity, the azimuthal shear, which is proportional to one-half the vertical vorticity, was estimated using the two-dimensional, linear least-squares derivative methodology developed in Smith and Elmore (2004), later improved in Miller et al. (2013) and Mahalik et al. (2019). The key advantage of this method in this case is its tolerance to noise resulting from any range gates not adequately corrected in the previous step. Before performing the derivatives to estimate the azimuthal shear, range gates where $Z_H < 20$ dBZ were masked, as these could result in noisy estimates in areas of low signal-to-noise ratio. This was followed by the application of a 3 × 3 median filter in azimuth and range to v_r to remove any additional noise. Given the lower resolution of the SNTG radar, a 1500 m × 4000 m kernel was utilized in the calculations (Mahalik et al. 2019), with the minimum number of range gates within the kernel needed for the estimates set to 5 due to instances of significant censoring of v_r by the radar processor being observed in some sweeps.

2.2 Storm tracking

To depict the life cycle of the supercell, the storm was tracked using the SNTG radar data. Storm tracking was performed after reading every radar volume using the Py-ART Python toolkit (Helmus and Collis 2016). The range gates were converted from their native polar coordinate system into a Cartesian coordinate system, with storm cores defined as regions where Z_H > 40 dBZ. Storm core objects that exceed a minimum volume of 3000 km^3 were then identified using SciPy's scipy.ndimage.label() function (Virtanen et al. 2020) and tracked using the TrackPy tracking package (Allan et al. 2025). Table 1 presents and describes each parameter extracted during storm tracking.

Table 1 Tracked storm parameters

Parameter	Description
storm id	Storm object identification number
x (m)	*X*-axis storm centroid coordinate
y (m)	*Y*-axis storm centroid coordinate
z (m)	*Z*-axis storm centroid coordinate
time (UTC)	Radar volume time
zh_volume (km^3)	Storm 40-dBZ volume
vil (kg km^{-2})	Storm mean of the 10 highest VIL values
echo top18 (km)	Storm 18-dBZ echo tops
echo top40 (km)	Storm 40-dBZ echo tops
vild (kg km^{-3})	Storm mean of the 10 highest VILD values
posh (%)	storm mean of the 10 highest POSH values
mesh (cm)	Storm mean of the 10 highest MESH values
az shear (s^{-1})	Storm mean of the 10 lowest azimuthal shear values

2.3 Satellite, lightning, and reanalysis datasets

The Geostationary Operational Environmental Satellite 13 (GOES-13) visible and infrared channels were used in conjunction with the automated weather stations (AWSs) from Brazil's National Institute of Meteorology (INMET, acronym in Portuguese) to analyze the supercell and its mesoscale environment during its early stages. The AWS hourly data include air and dewpoint temperatures at 2 m above ground level (AGL), wind speed and direction at 10 m AGL, pressure, and precipitation rate. The mesoscale environment was also analyzed using the upper-air data from the Santa Maria (SBSM; 29.7°S–53.7°W; elevation: 85 m) and Uruguaiana (SBUG; 29.8°S–57.9°W; elevation: 74 m) stations. The spatial distribution of AWSs and rawinsonde stations is shown in Fig. 1b.

Variations in storm intensity were also analyzed using data from Brazilian Integrated Lightning Detection Network Lightning (RINDAT, acronym in Portuguese). RINDAT sensors detect cloud-to-ground (CG) and intracloud (IC) lightning flashes by mapping very low frequency/low frequency (VLF/LF) radiation emissions using time-of-arrival direction magnetic finder techniques to determine the time, location, peak current, polarity of each flash, and multiplicity (Pinto et al. 2006). The temporal resolution achieved by the network is 300 ns (Luz 2015), with an average location accuracy of 500 m, and with the detection efficiency for events occurring within the network coverage (Machado et al. 2009).

In addition, six-hour operational global analyzes from the National Centers for Environmental Prediction (NCEP) Climate Forecast System version 2 (CFSv2; Saha et al. 2014) were used to evaluate the synoptic-scale environment preceding the formation and during the life span of the SVS supercell. CFSv2 has data at 0.5° horizontal resolution and at 37 isobaric levels, including 9 levels in the 1000 − 800 hPa layer. The computation of convective parameters from CFSv2 and observed upper-air data was performed using the Sounding and Hodograph Analysis and Research Program in Python (SHARPpy; Blumberg et al. 2017).

3 Synoptic- and mesoscale setup

3.1 Synoptic-scale features

In the mid-afternoon of 6 October 2015 (1500 LST or 1800 UTC), ~ 1 h before the formation of the original (pre-merger) supercell, the 250-hPa flow displayed an anticyclonically curved jet over SB, whose 70 + m s^{-1} streak was located upstream in the Andes around 33°S (Fig. 2a). This jet stream was associated with a trough in the Pacific Ocean that was approaching the Andes mountains. At 500 hPa (Fig. 2b), the ridge's axis was displaced to the east of RS, southward of an anticyclone situated at the border between Brazil and Paraguay (21.50°S–57.00°W). This flow configuration placed western RS under westerly-southwesterly flow, which strengthened rapidly from 500 hPa (~15 m s^{-1}; Fig. 2b) to 200 hPa (~40 m s^{-1}; Fig. 2b). In the lower troposphere, a pre-cyclogenesis pattern was in place (Lopes and Nascimento 2024) (Fig. 2c). A northwesterly low-level jet (LLJ) was located in a sharp geopotential height gradient associated with a lee low just east of the Andes, known as the Northwestern Argentinean Low (NAL) (Seluchi et al. 2003). At the surface (Fig. 2d), the NAL extended southeastward across Uruguay towards the South Atlantic ocean as an inverted trough, with cool southerly winds to its south in central Argentina and north-northeasterly winds on its east side, in extreme northeastern Argentina and RS. The ensuing frontogenetic pattern contributed to the advection

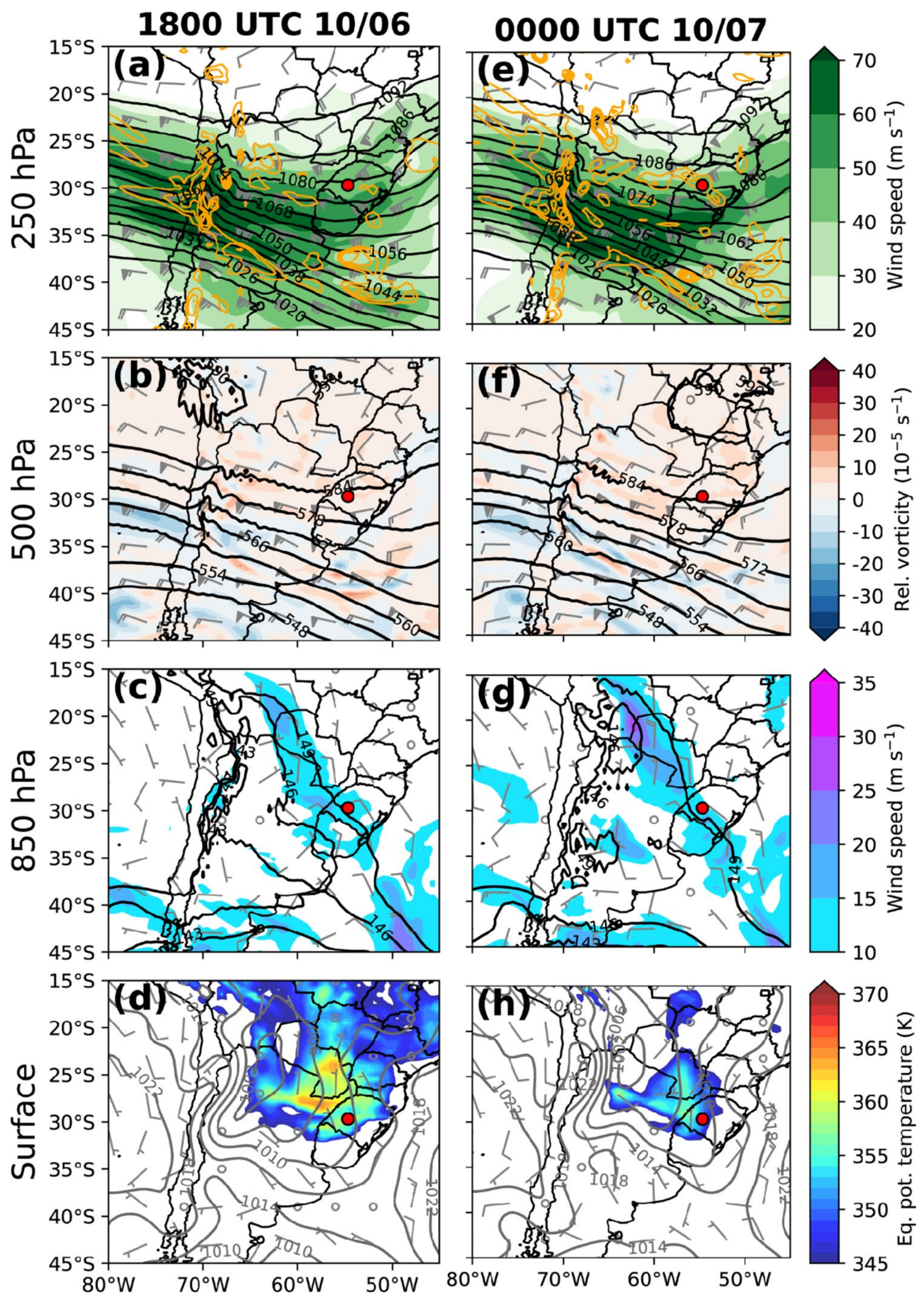

Fig. 2 CFSv2 synoptic charts for the (left column) 1800 UTC 6 October (right column) and 0000 UTC 7 October 2015. (**a, e**) 250-hPa geopotential heights (dam; black contours), horizontal winds (m s^{-1}; barbs), and divergence (×10^{-5} s^{-1}; orange contours every 2 × 10^{-5} s^{-1}, starting at 2 × 10^{-5} s^{-1}). (**b, f**) 500-hPa geopotential heights (dam; black contours), winds (barbs), and relative vorticity (×10^{-5} s^{-1}; shaded). (**c, g**) 850-hPa geopotential heights (dam; black contours), winds (barbs), and wind speed (m s^{-1}; shaded). (**g, h**) 2-m AGL equivalent potential temperature (K; shaded), pressure reduced to mean sea level (hPa; dark gray contours), and 10-m AGL winds (barbs). Black contours in the background outline South America and its geopolitical boundaries. Wind barbs depict the following: half barbs = 5 m s^{-1}; full barbs = 10 m s^{-1}; flags = 25 m s^{-1}. The red circle shows the location of SVS

of warm, moisture-rich air from the Amazon poleward into southern Paraguay, northeastern Argentina and west-central RS, contributing to a pool of high equivalent potential temperature (θ_e) seen in Fig. 2d.

At 0000 UTC 7 October 2015, around the time the postmerger supercell dissipated, RS remained to the north of the upper-level jet as it moved around the base of the ridge (Fig. 2e). Some areas of localized divergence developed in central RS at 0000 UTC, but these may be associated with CFSv2-parameterized convection given the lack of clear background divergent wind field associated with the jet (Oliveira et al. 2025). The accompanying midlevel jet considerably strengthened the 500-hPa winds over west RS to 20–25 m s^{-1}, while geopotential heights slightly increased, suggesting a negligible contribution from midlevel quasi-geostrophic dynamics (Fig. 2f). Hence, the role of the midlevel jet was to provide strong vertical shear that was necessary for supercellular convection. In addition, the NAL-related trough shifted toward the coast of Uruguay, focusing the axis of the LLJ over southwestern RS (Fig. 2g). The approach of the surface trough in northern Argentina and Uruguay increased the easterly component of the winds in west-central RS, where the high θ_e pool became established (Fig. 2h).

3.2 Mesoscale environment, storm formation, and early evolution

Figure 3 shows GOES-13 visible imagery and AWS observations of the environment during the initiation and early phase of the original supercell. At 1907 UTC (Fig. 3a), the initial convection that would eventually evolve into the original supercell had just formed in western RS in a growing cumulus field under clear skies, with surface temperatures exceeding 30 °C and dewpoints greater than 20 °C (Fig. 3b). At this initial stage, the STNG radar detected a small cell with $Z_H > 35$ dBZ, moving southeastward (Fig. 3a). Amidst the developing cumulus field were some additional cells with long anvils within bands of stratus ("billow") clouds, which were more prevalent near the border with Uruguay and into Argentina near the axis of the LLJ (Fig. 2c), suggesting the presence of a capping inversion. To the south, clear skies prevailed, despite relatively high surface temperatures and dewpoints (Fig. 3a, b), further indicating that the air mass was strongly capped.

In the following hour, the storm matured and strengthened significantly. The storm developed characteristics of a "classic" supercell, such as a hook-like appendage, an elongated forward-flank downdraft (FFD) region, and very long southwest-northeast-oriented anvils (Fig. 3c) due to the strong upper-level winds (Fig. 2a). In addition, storm motion changed from southeastward to east-northeastward as the storm increasingly deviated to the left of the deep-layer shear vector in consistency with left-moving, cyclonic supercells in the Southern Hemisphere (Nascimento et al. 2014; Oliveira et al. 2022, 2025; Ferreira et al. 2022; Piscitelli et al. 2022; Lopes et al. 2025).

The above analysis suggests that the original supercell formed within a capped environment. Given the high surface temperatures and dewpoints, strong diurnal heating likely allowed surface-based parcels in western RS to attain their convective temperatures, thereby substantially reducing convective inhibition (CIN). However, given the presence of the cap, localized lifting was likely still required to initiate deep convection. Although not clearly observed in Fig. 3, strong differential heating over the complex terrain of western RS (Fig. 1b) may have enhanced terrain-induced circulations that favored storm initiation. Previous studies have shown that even modest orography can promote deep convection through thermally driven circulations under strong surface heating (Soderholm et al. 2014; Nisi et al. 2018; Nelson et al. 2022). In addition, the complex orography of western RS may have generated boundary-layer convergence zones within valleys and along terrain-induced circulations (Kirshbaum et al. 2018; Katona and Markowski 2021), providing localized ascent capable of overcoming the remaining CIN. Consistent with this interpretation, Liu and Kirshbaum (2026) showed that boundary-layer convergence lines produce deeper, wider, and more densely packed convection than that initiated by ordinary boundary-layer turbulence.

The role played by capping inversions and CIN in the development of severe storms in SB has remained uncertain. On one hand, in situations where a robust EML is present, the capping inversion at its base can increase CIN and help to suppress widespread convective development, favoring isolated and/or semi-discrete supercell modes with strong updrafts (due to steep lapse rates), such as in "classic" severe weather setups in the U.S. Great Plains (Ribeiro and Bosart 2018). On the other hand, when EMLs are weak or absent, pre-storm environments are susceptible to generalized storm formation. An evaluation of the 1200 UTC 6 October SBUG sounding does show a sharp temperature inversion between ~660–690 hPa at the base of an EML (Fig. 4a) under northwesterly low-to-mid-level flow (see hodograph inset in Fig. 4a), in consistency with known EML storm environments for this sector of SB (Ribeiro and Bosart 2018). Given the depth of the moist layer (~3 km) and that convective temperatures (~30 °C) were exceeded in the afternoon in western RS (Fig. 3b), the original storm likely formed along boundary-layer circulations fostered by intense diurnal heating.

The capping inversion is also evident in the 0000 UTC 7 October 2015 SBSM sounding (Fig. 4b) near the location

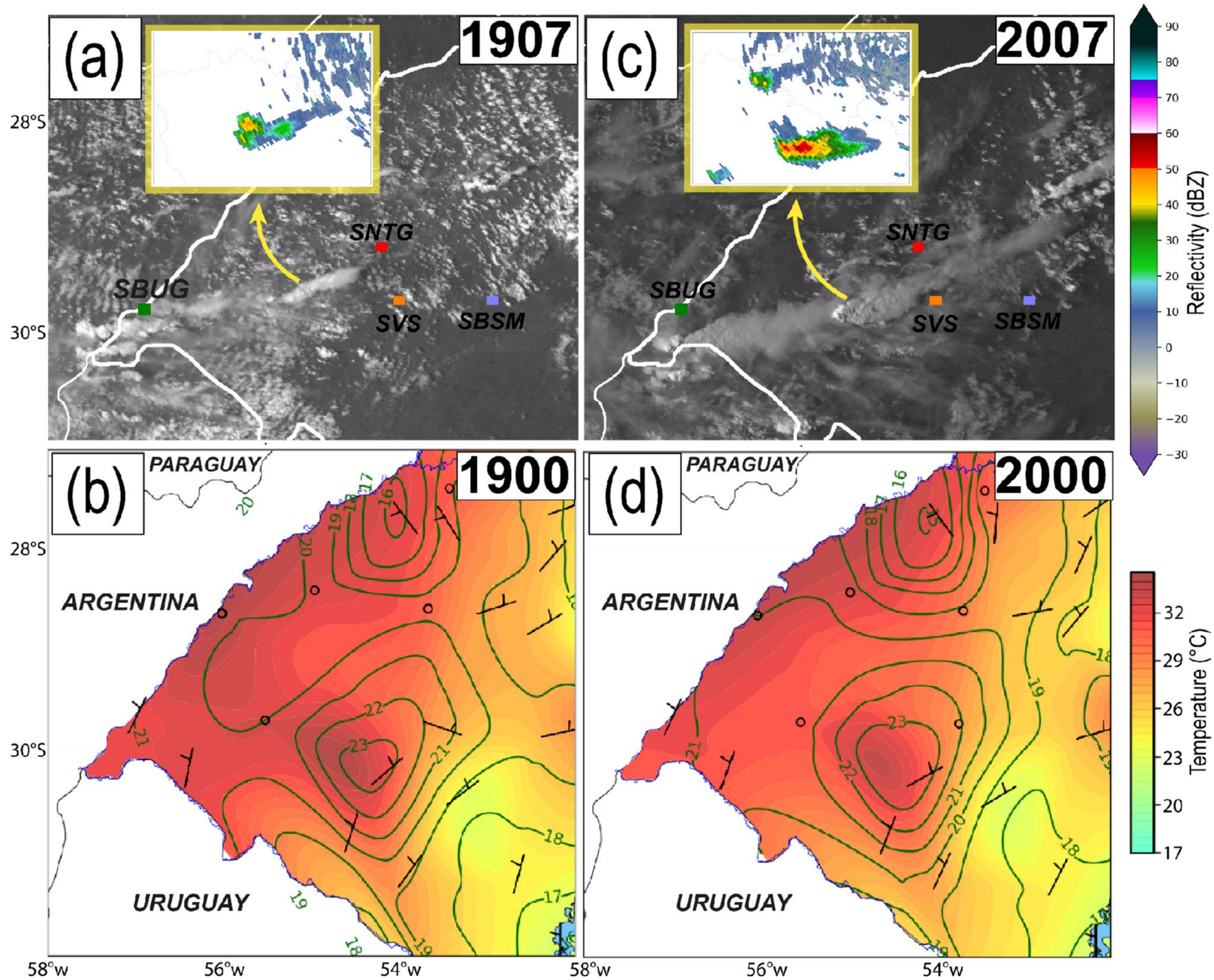

Fig. 3 GOES-13 visible imagery (first row) and the corresponding AWS observations (second row) over west-central RS at (**a**) 1907 UTC, (**b**) 1900 UTC, (**c**) 2007 UTC, and (**d**) 2000 UTC 6 October 2015. In (**a**) and (**c**), thin white contours outline RS, the purple and green squares represent SBSM and SBUG, respectively. The red and orange circles indicate STNG and SVS, respectively. The insets in (**a**) and (**c**) show STNG 0.5° PPI Z_H (dBZ) at (**a**) 1910 UTC and (**c**) 2010 UTC 6 October 2015. (**b**) and (**d**) show the 2-m AGL temperature at 2 m AGL (color shaded), dewpoint (green contours, every 1 °C), and 10-m AGL winds (barbs; half barb is 5 m s^{-1}, and open circle denotes calm winds). The barb and open circle positions indicate AWS locations

where the postmerger supercell dissipated. The SBSM thermodynamic profile shares many similarities with the morning SBUG profile: it has comparable LCLs, LFCs, a moist layer depth of ~3 km, but higher CAPE due to the heated boundary layer. Although the SBSM profile contains weaker capping at 3 km AGL, it also has increased stability due to the early evening conditions and some drying below 1 km AGL, which result in stronger CIN values (-98 J kg^{-1}) than those observed at SBUG (-29 J kg^{-1}). The enhanced inhibition at SBSM may have played a role in the dissipation of the postmerger supercell, as will be discussed later. The drying at SBSM is linked to interactions between the east-northeasterly near-ground winds from the higher terrain just north of SBSM (Fig. 1b), as discussed in prior studies (Rosa et al. 2022).

The effective bulk wind difference (EBWD) was favorable for supercells (around 50 kt or 25 m s^{-1}; 1 kt = 0.514 m s^{-1}) as seen in the long hodographs at SBUG and SBSM (Fig. 4). The northeasterly winds below 1 km AGL under the LLJ aloft promoted ample counterclockwise curvature and large ESRH of nearly −400 m^2 s^{-2} at SBSM (Fig. 4b), more than enough to sustain strong mesocyclones and long-lived supercells (Bunkers et al. 2006a, b).

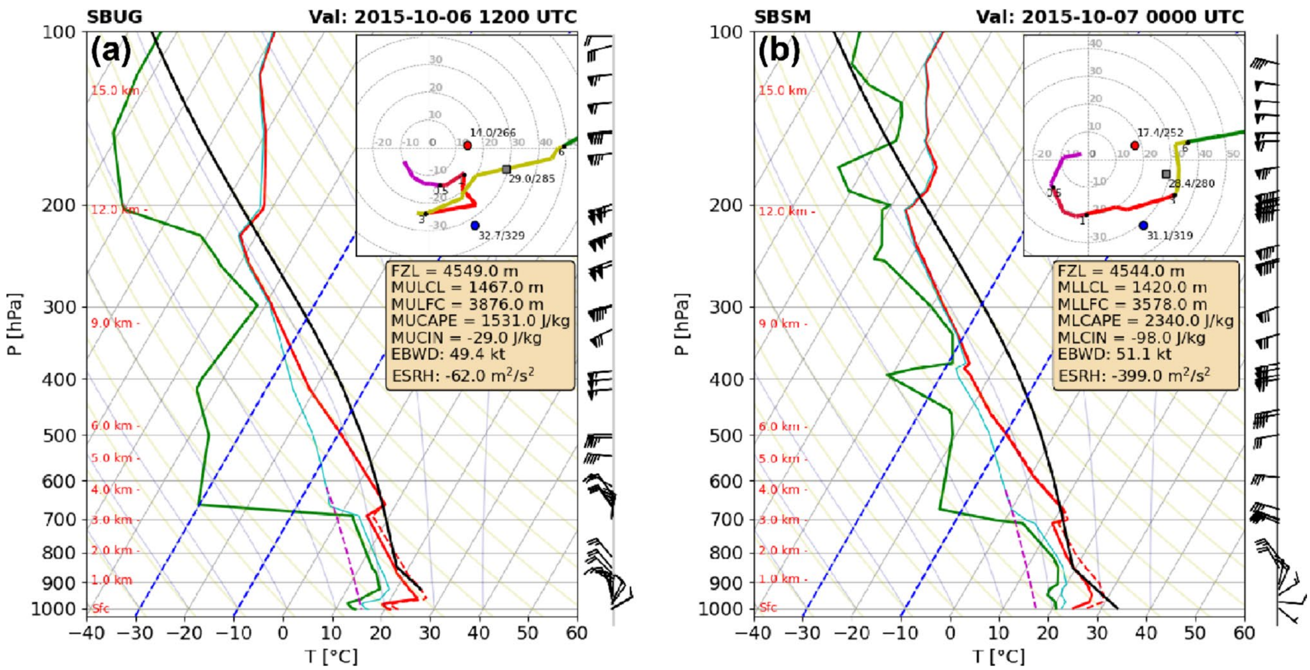

Fig. 4 Observed soundings at SBUG and SBSM at (**a**) 1200 UTC 6 October and (b) 0000 UTC 7 October 2015, respectively. The thermodynamic profile is shown as a skew-*T*-log-*p* diagram, with red, green and solid back lines denoting the temperature, dewpoint, and (**a**) most unstable (MU) and (**b**) 100-hPa mixed layer (ML) parcel ascent curves, respectively. The wind profile is shown as hodographs in the top-right corner of (**a**) and (**b**), with 0-0.5, 0.5-1, 1–3, 3–6, and 6–10 km AGL winds represented as magenta, dark red, red, olive, and green line segments, respectively. Winds are in m s^{-1}. A few relevant convective parameters are included in the inset below the hodograph. For both figures, these include the height of the freezing level (FZL), the effective bulk wind difference (EBWD), and effective storm-relative helicity (ESRH). The lifting condensation level (MULCL and MLLCL), level of free convection (MULFC and MLLFC), convective available potential energy (MUCAPE and MLCAPE), and convective inhibition (MUCIN and MLCIN) are shown for the most unstable and mixed-layer parcels in (**a**) and (**b**), respectively

3.3 Merger with nascent supercell and subsequent storm intensification

As the original supercell moved into central RS, a few smaller cells formed ~ 30–40 km to its northwest and north (Fig. 5a, b). The cells farther northwestward decayed rapidly, presumably due to entrainment in the capped environment. However, a single nascent cell that formed ~ 30 km to the north of the original supercell persisted and strengthened, developing into an elongated reflectivity segment (Fig. 5c, d) that is consistent with the nascent supercells analyzed in the numerical study of Hastings and Richardson (2016). The nascent cell moved southward and collided with the original supercell at 2140 UTC (Fig. 5e, f).

Figure 6 presents a focused view of the cell merger and the subsequent storm evolution at 10-min intervals. The merger began at 2150 UTC, when the northern end of the nascent supercell's forward flank began to connect with that of the original supercell (Fig. 6a-d). The consolidation of the merger process occurred at 2200 UTC, when the core of the nascent supercell, defined by the 35-dB*Z* outline at the lowest PPI, merged with the core of the original supercell to form a single, larger storm (Fig. 6e-h), in consistency with the definition of supercell merger of Flournoy et al. 2022. The merger evolution shown in Fig. 6a and e resembles both the "updraft collision" and "forward-flank merger, resulting in the dissipation of the original cell" scenarios presented in the idealized simulations of Hastings and Richardson (2016). In the former scenario, the updraft cores first connect via an updraft bridge and subsequently merge. The original updraft then weakens, as inflow parcels are redirected into the strengthening updraft of the nascent cell, which evolves into a classic or HP supercell. In the latter scenario, the nascent cell's outflow undercuts the original supercell's inflow, causing its dissipation. As in the updraft collision scenario, the nascent cell becomes the dominant supercell. A definitive conclusion about the exact type of merger observed in the 6 October 2015 storm based on Hastings and Richardson's (2016) model is difficult, given the long volume update interval of the SNTG radar. Regardless of the exact type of merger, Fig. 6 strongly suggests that the merger caused the nascent cell to evolve into the dominant supercell, which became significantly stronger than either of its predecessors.

Interestingly, during the merger (Fig. 6a-f), the original supercell developed a prominent dual-appendage structure

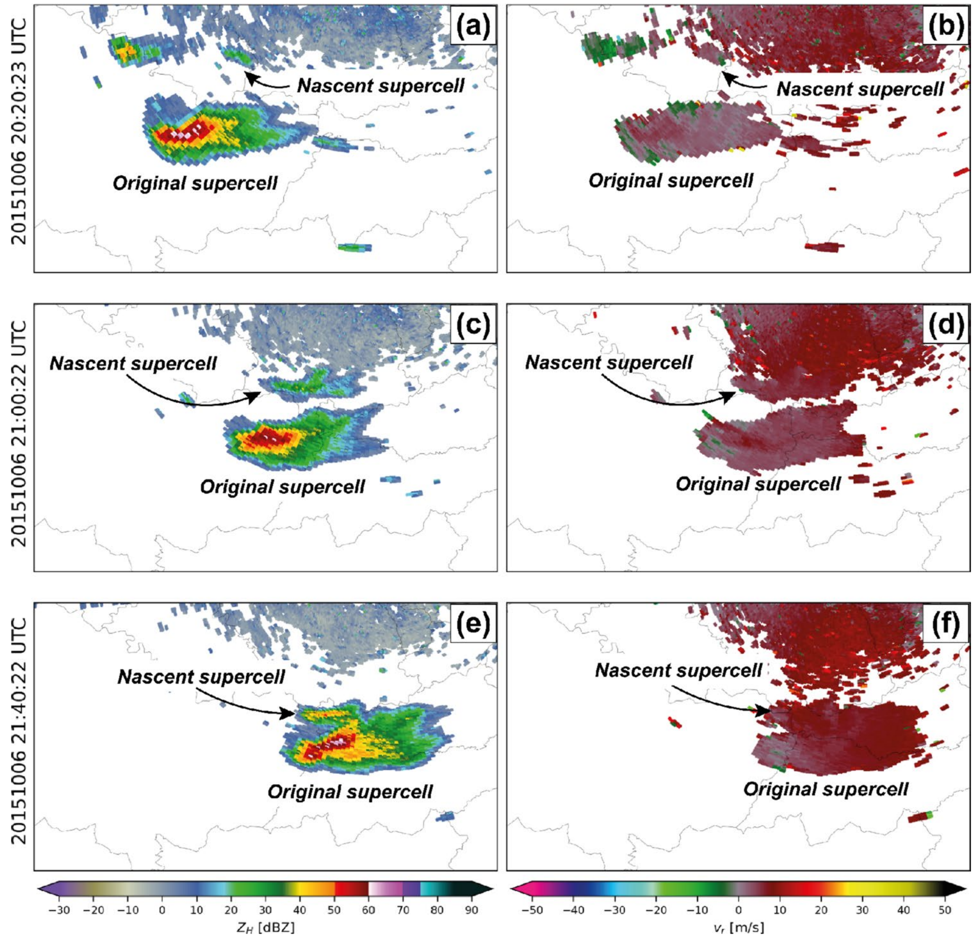

Fig. 5 STNG 0.5° PPIs of (**a, c, e**) Z_H (dB*Z*) and (**b, d, f**) v_r (m s^{-1}). Thin black lines indicate county borders. The times in each row from the top to the bottom panels are (**a**), (**b**) 2020:23, (**c**), (**d**) 2100:22, and (**e**), (**f**) 2140:22 UTC 6 October 2015

in its rear flank resembling the "Owl Horn Signature" (OHS) described by Kramar et al. (2005), occasionally observed in low-level PPIs of developing supercells. OHSs may develop as the head of the storm's rear-flank cold pool interacts with both environmental and storm-generated horizontal vorticity, producing vertical vortex couplets that extend precipitation into long, narrow bands on the storm's rear flank. These features are often precursors of supercell intensification and storm splitting (Kramar et al. 2005), which aligns with the observed reflectivity structure of the original supercell in Fig. 6a, e. Given that OHSs depend on the interaction between cold pools and near-surface horizontal vorticity, it is possible that the merger reinforced the rear-flank outflow of the original supercell and generated the vorticity couplets necessary for OHS formation.

During and immediately after the merger, the postmerger supercell intensified dramatically. The intensification is evident in the increasing Z_H in the storm's core to ~70 dB*Z* (Fig. 6e, i), strengthening of the low-level mesocyclone (Fig. 6f, j), increase in ETs of ~3 km (from 12 to 15 km) (Fig. 6g, k), and expansion of the VILD area in excess of 15 kg m^{-3} (Fig. 6h, l). These increases indicate that the merging updrafts evolved into a much wider and stronger midlevel updraft capable of suspending larger concentration hydrometeors at higher altitudes. The appearance of a BWER in the 7° PPI is direct evidence of the stronger midlevel updraft (Fig. 7a). The mesocyclone continued to strengthen into a vertically deep column, with collocated inbound-outbound v_r couplets at the 0.5° and 7° PPIs (Figs. 6n and r and 7b, respectively) collocated with a hook echo (Fig. 6m, q). Furthermore, the intensifying midlevel mesocyclone caused the storm motion to shift from east-northeastward to northeastward. This storm motion placed SVS near the 70 + dB*Z* core of the supercell at 2230 UTC, where hail of 6 + cm diameter was reported for the first time during the storm's life cycle. These in situ large hail observations match well the ET (Figs. 6k, o and s and 7c), VILD (Figs. 6k, o and s and 7d), POSH (Fig. 7e), and MESH (Fig. 7f) estimates from the SNTG radar (Amburn and Wolf 1997; Murillo and Homeyer 2019).

A quantitative assessment of storm evolution and its relationship with the merger is presented in Fig. 8. Two key periods of rapid storm evolution are evident in Fig. 8: the intensification phase associated with the merger (2200 to 2230 UTC) and the weakening phase (2230 to 2300 UTC). The effect of the merger on updraft intensification is clear in

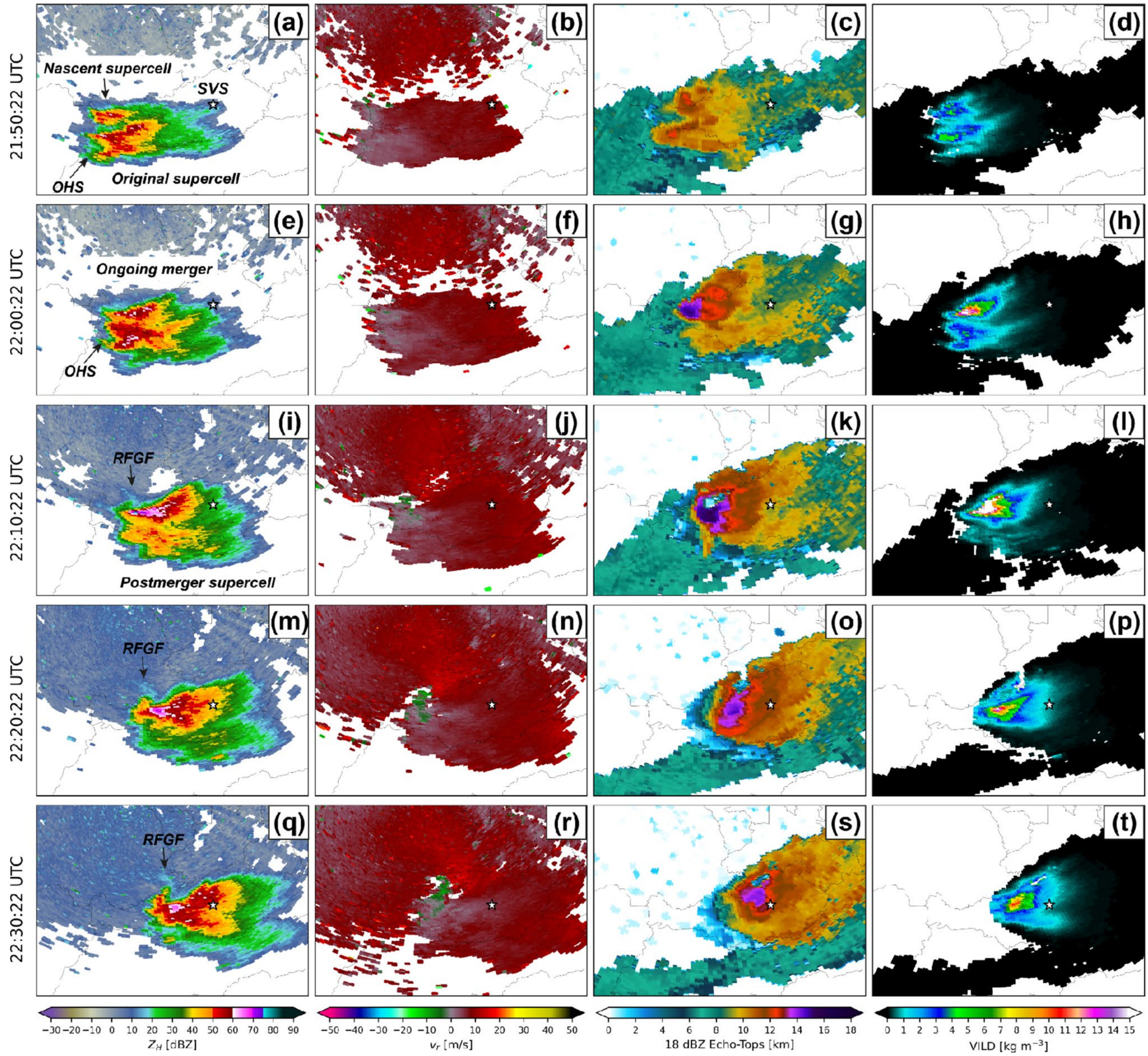

Fig. 6 SNTG 0.5° PPIs of (**a, e, i, m, q**) Z_H (dBZ), (**b, f, j, n, r**) v_r (m s^{-1}), (**c, g, k, o, s**) 18-dBZ ETs (km), and (**d, h, l, p, t**) VILD (kg m^{-3}). The times in each row from the top to the bottom panels are (**a-d**) 2150:22, (**e-h**) 2200:22, (**i-l**) 2210:22, (**m-p**) 2220:22, and (**q-t**) 2230:22 UTC 6 October 2015. The star indicates the location of SVS

Fig. 8a, as the ET of the 18-dBZ (40-dBZ) isosurface deepens by ~3 km (~5 km) within 30 min of the merger, producing an overshooting top well above the equilibrium level shown in Fig. 4b in the SBSM sounding. The stronger and wider updraft/mesocyclone of the postmerger produced much stronger mass fluxes and vertical accelerations that contributed to a 250% expansion of the storm volume (Fig. 8b), a 320% sudden increase in VILD (Fig. 8c), a 230% increase in the magnitude of the 2-5-km azimuthal shear (Fig. 8d), and a 680% "jump" in the lightning flash rate. The occurrence of a "lightning jump" (Schultz et al. 2009) particularly when accompanied by other radar indications of updraft strengthening, points to imminent severe weather, as was confirmed in this case via reports of large hail. In fact, the reports of large hail occurred within 45 min of the merger, after which time the updraft of the postmerger supercell matured and was able to sustain large hailstones. The occurrence, timing, and size of the large hail reports match well the maximum POSH and MESH estimates (Fig. 8e and f, respectively).

The weakening phase of the postmerger supercell occurred as it moved across central RS. The sharp drop in the total lightning flash rate (from 70 to less than 10 flash min^{-1}) during the 2300–2330 UTC period slightly leads or

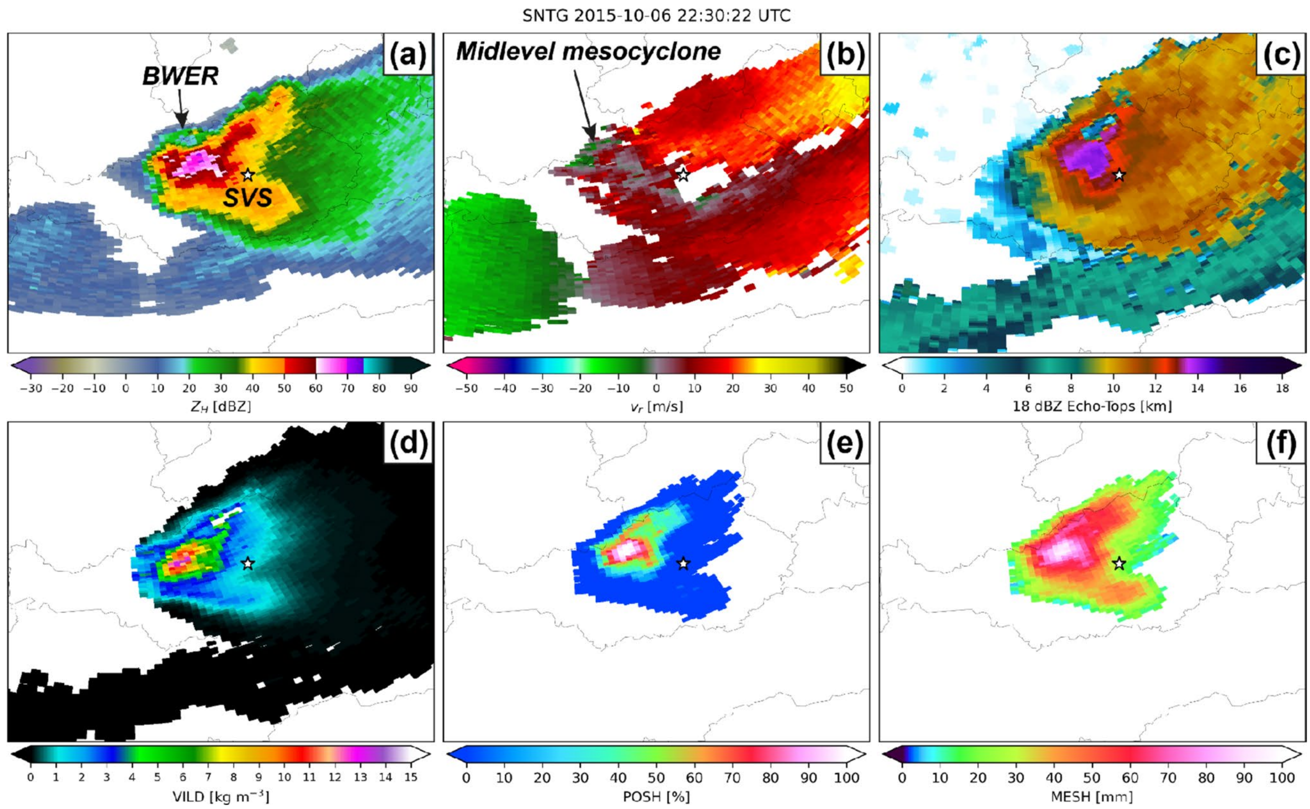

Fig. 7 (**a**) STNG 7° PPI of Z_H (dB*Z*), (**b**) v_r (m s^{-1}), (**c**) 18-dB*Z* ETs (km), (**d**) VILD (kg m^{-3}), (**e**) POSH (%), and (**f**) MESH (mm). The arrows denote, respectively, the (**a**) BWER and the (**b**) midlevel mesocyclone. Fields valid at 2230:22 UTC 6 October 2015

lags by 10 min the trends in all quantities shown in Fig. 8 and occurs around 2250 UTC. In all, Fig. 8 suggests that rapid changes in the mesoscale environment or internal storm-scale process drastically weakened the updraft of the postmerger supercell. As discussed in Sect. 3.2, the 0000 UTC 7 October SBSM proximity sounding displayed a capping inversion at ~3 km AGL and relatively cool, dry near-surface layers, which contributed to robust MUCIN. In addition, Fig. 9a, e,i show an RFGF surging from the hook echo as a fine line leading to a growing area of inbound v_r < -10 m s^{-1} (Figs. 9b, f,j). The appearance of the surging RFGF after the significant hailfall event shown in Figs. 7 and 8 and shortly before the decaying phase of the storm is an indication that the merger abruptly strengthened the rear-flank downdraft (RFD) of the postmerger supercell. Moreover, additional evidence for a stronger RFD is inferred from the appearance of a new OHS in Figs. 9b, f,j. Given the stronger RFD together with the drier environment seen in the proximity sounding, it is possible that the postmerger supercell rapidly weakened and dissipated in central RS because it moved into a drier, stable environment during an episode of hailfall caused by the merger, which reinforced the outflow and cut off of the updraft/mesocyclone from the conditionally unstable environment, as discussed by Bluestein (2008), van den Broeke et al. (2023), and Pardun et al. (2026). In other words, despite the presence of high shear and instability in central RS, it seems that the merger-induced hailfall promoted a stronger cold pool that cut off the supply of unstable air into the updraft and increased the already strong MUCIN for air parcels from the storm's outflow, thus suppressing the ability of the mesocyclone to dynamically lift the stable low-level air parcels to their LFC. As with the OHS described earlier, a closer inspection of the mechanisms causing the rapid decay of the postmerger supercell warrant numerical simulations.

4 Summary and conclusion

This study documented the lifecycle and storm environment of a large-hail producing supercell observed on 6 October 2015 in west-central RS. Emphasis was given to a merger between the original supercell and a nascent supercell, which preceded storm intensification and the onset of reports of 6+cm hailstones. The synoptic- and mesoscale environment prevalent on 6 October 2015 was conducive to isolated classic supercells. Both the original (premerger) and nascent supercells developed in a pre-cyclogenesis scenario typical of SB severe storm environments, in which a northwesterly LLJ supplied warm, moist air from the

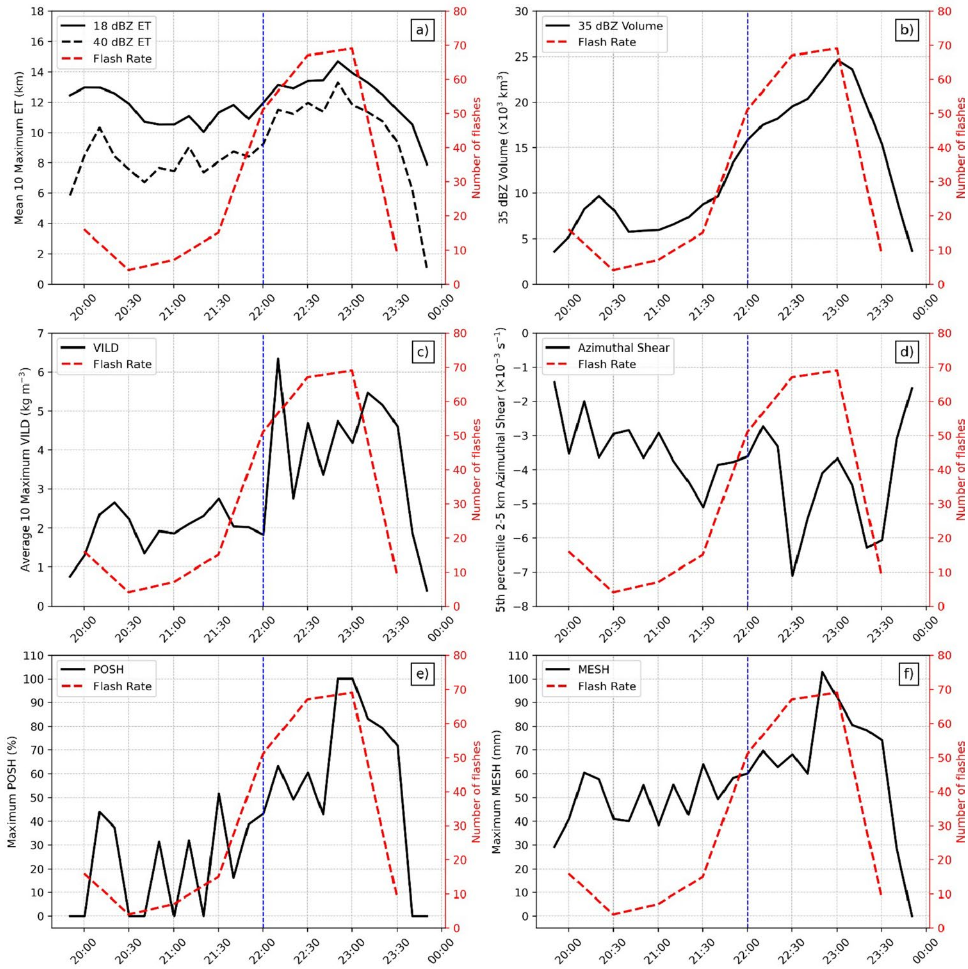

Fig. 8 Time series of tracked storm metrics: (**a**) mean of 10 maximum range gate values of 18- and 40-dB*Z* ETs (km), (**b**) total 35-dB*Z* volume, (**c**) mean of 10 maximum range gate values VILD (kg m^{-3}), (**d**) 5th percentile of the 2–5 km azimuthal shear (s^{-1}), (**e**) maximum POSH (%), and (**f**) maximum MESH (mm). The red dashed line in all panels indicates the number of flashes detected by the RINDAT network. The dashed blue line at 2200 UTC indicates the time of the merger

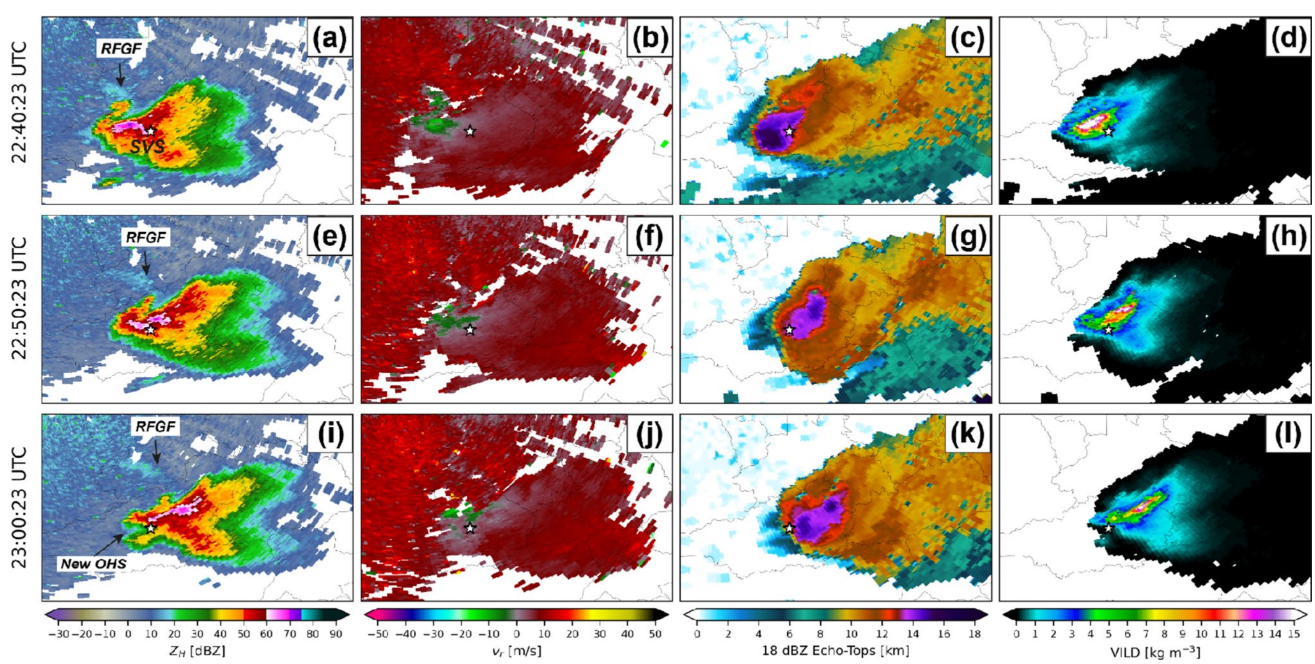

Fig. 9 Same as Fig. 6, but at (**a**), (**b**) 2240:23, (**c**), (**d**) 2250:23, and (**e**), (**f**) 2300:23 UTC 6 October 2015. Also, the RFGF and new OHS are denoted by black arrows in (**a, e, i**) and (**i**), respectively

Amazon basin to west-central RS, where strong upper-level winds were in place. Upper-air soundings in west and central RS indicated that a robust EML around 3 km AGL prevented widespread convection initiation in the warm advection regime, but supported isolated storm formation in locations where surface-based parcels reached their convective temperatures. The combination of strong instability, steep lapse rates, and ample vertical wind shear contributed to supercellular convection. Compared to other case studies of supercells in SB (Oliveira et al. 2022; Ferreira et al. 2022; Lopes and Nascimento 2024; Lopes et al. 2025), this event is likely the one that best illustrates the potentially constructive effects that the presence of an EML may exert in environments in which they occur less frequently (Ribeiro and Bosart 2018).

The merger between the original and the nascent supercell was likely key to producing a storm that was more severe than its predecessors. In this sense, the merger resembles both the "updraft collision" and "forward-flank merger, resulting in dissipation of the original cell" processes described by Hastings and Richardson (2016). Following the merger, the storm developed numerous signatures on radar characteristic of intensifying supercells, including a distinctive hook echo, a surging RFGF, a BWER, and even an "Owl Horn Signature (OHS)". More importantly, the merger produced a sudden intensification of the updraft and mesocyclone in the postmerger supercell, which caused a significant episode of hailfall that matched well the radar-estimated and surface observations of large hail. The same hailfall event was hypothesized to cause the demise of the supercell, as the storm encountered a drier environment in central RS, which helped strengthen the supercell's outflow and cut off its access to unstable inflow. Overall, not only this case illustrates the potential constructive effects that cell mergers have on the short-term evolution of supercells, but also the destructive effects it may cause later during the life cycle of the storms. Forecasters should be particularly aware of the potential and implications of cell mergers for nowcasting purposes, as rapid changes in storm behavior are expected. This is particularly challenging in SB, given that radar volume update times are relatively long and the typical outcomes of cell mergers are yet to be studied.

Although the 6 October 2015 supercell case features an interesting merger event, a deeper understanding of the role played by cell mergers in storm evolution in SB requires analysis of a large sample of events. Research using the PREVOTS (Portuguese for Platform for Severe Weather Reports and Storm Spotter Network; Ribeiro et al. 2022) severe weather database is currently underway and will the assess statistics of cell mergers for a variety storm modes, including supercells. Based on these results, numerical simulations of select events can be used to investigate the dynamics of cell mergers and its impacts on storm evolution in a future study.

Acknowledgements The authors thank the anonymous reviewer and the editor for the thorough and constructive suggestions, which helped improve the article significantly. Dr. Thiago Bíscaro is thanked for providing the raw radar data used in this study. Fruitful discussions with Dr. Howard B. Bluestein at the University of Oklahoma about the "Owl Horn Signature" helped clarify its existence in the available radar data. The first author is grateful for the funding support provided by the Coordenação de Aperfeiçoamento de Pessoal de Nível Superior (CAPES) during his PhD at the School of Meteorology of the University of Oklahoma.

Author contributions All authors contributed to the study conception and design. Material preparation and data collection by Maurício I. Oliveira and data analysis was performed by all authors. Vitor Goede and Eliton L. Figueiredo were responsible for most figures. The first draft of the manuscript was written by Maurício I. Oliveira and all authors commented on previous versions of the manuscript. All authors read and approved the final manuscript.

Funding The Article Processing Charge (APC) for the publication of this research was funded by the Coordenação de Aperfeiçoamento de Pessoal de Nível Superior - Brasil (CAPES) (ROR identifier: 00x0ma614). This work is part of the first author's PhD work, supported by the Coordenação de Aperfeiçoamento de Pessoal de Nível Superior (CAPES) from the Brazilian Ministry of Education, Grant number 88881.129505/2016-01 of the "Programa de Doutorado Pleno no Exterior" (DPE – 3830).

Data availability The datasets generated and analyzed during this study are available upon reasonable request to mauricio.meteorologia@gmail.com.

Declarations

Competing interests The authors declare no competing interests.

References

Alford AA, Biggerstaff MI, Ziegler CL, Jorgensen DP, Carrie GD (2022) A method for correcting staggered pulse repetition time (PRT) and dual pulse repetition frequency (PRF) processor errors in research radar datasets. J Atmos Ocean Technol 39(11):1763–1780. https://doi.org/10.1175/JTECH-D-21-0176.1

Allan DB, Caswell T, Keim NC, van der Wel CM, Verweij RW (2025) Soft- matter/trackpy: Trackpy v0.5.0. Zenodo. https://doi.org/10.5281/zenodo.16089574

Amburn SA, Wolf PL (1997) VIL density as a hail indicator. Weather Forecast 12(3):473–478. https://doi.org/10.1175/1520-0434(1997)012%3C0473:VDAAHI%3E2.0.CO;2

Bechis HB, Ribeiro BZ, Cancelada M, Salio P, Ruiz J, Granato A, Saucedo M (2025) Environments associated with hail and convectively generated damaging wind gusts in South America. Q J R Meteorol Soc e5029. https://doi.org/10.1002/qj.5029

Bluestein HB (2008) On the Decay of Supercells through a Downscale Transition: Visual Documentation. Mon Weather Rev 136(10):4013–4028. https://doi.org/10.1175/2008MWR2358.1

Blumberg WG, Halbert KT, Supinie TA, Marsh PT, Thompson RL, Hart JA (2017) SHARPpy: An open-source sounding analysis toolkit for the atmospheric sciences. Bull Am Meteorol Soc 98(8):1625–1636. https://doi.org/10.1175/BAMS-D-15-00309.1

Bunkers MJ, Klimowski BA, Zeitler JW, Thompson RL, Weisman ML (2000) Predicting supercell motion using a new hodograph technique. Weather Forecast 15(1):61–79. https://doi.org/10.1175/1520-0434(2000)015%3C0061:PSMUAN%3E2.0.CO;2

Bunkers MJ, Hjelmfelt MR, Smith PL (2006a) An observational examination of long lived supercells. Part I: Characteristics, evolution, and demise. Weather Forecast 21(5):673–688. https://doi.org/10.1175/WAF949.1

Bunkers MJ, Johnson JS, Czepyha LJ, Grzywacz JM, Klimowski BA, Hjelmfelt MR (2006b) An observational examination of long-lived supercells. Part II: environmental conditions and forecasting. Weather Forecast 21(5):689–714. https://doi.org/10.1175/WAF952.1

Bunkers MJ, Wilson MB, Van Den Broeke MS, Healey DJ (2022) Scan-by-scan storm-motion deviations for concurrent tornadic and nontornadic supercells. Weather Forecast 37(5):749–770. https://doi.org/10.1175/WAF-D-21-0153.1

Chisholm AJ (1973) Alberta hailstorms Part I: Radar case studies and airflow models. J Atmos Ocean Technol 14:1–36. https://doi.org/10.1007/978-1-935704-32-41

Ferreira V, Goede V, Nascimento EL (2022) An environmental and polarimetric study of the 19 November 2015 supercell and multiple-vortex tornado in Marechal Candido Rondon, southern Brazil. Meteorol Atmos Phys 134(5):82. https://doi.org/10.1007/s00703-022-00922-5

Fischer J, Flournoy MD, Lyza AW (2023) Comments on A climatology of cell mergers with supercells and their association with mesocyclone evolution and The influence of cell mergers on supercell characteristics and tornado evolution on 27–28 April 2011. Mon Weather Rev 151:2541–2545. https://doi.org/10.1175/MWR-D-23-0120.1

Flournoy MD, Lyza AW, Satrio MA, Diedrichsen MR, Coniglio MC, Waugh S (2022) A climatology of cell mergers with supercells and their association with mesocyclone evolution. Mon Weather Rev 150(2):451–461. https://doi.org/10.1175/MWR5D-21-0204.1

Goede V (2022) Assinaturas polarimétricas em tempestades supercelulares no Sul do Brasil. Dissertation, Universidade Federal de Santa Maria

Hastings R, Richardson Y (2016) Long-term morphological changes in simulated supercells following mergers with nascent supercells in directionally varying shear. Mon Weather Rev 144(2):471–499. https://doi.org/10.1175/MWR-D-15-0193.1

Helmus JJ, Collis SM (2016) The Python ARM Radar Toolkit (Py-ART), a library for working with weather radar data in the Python programming language. J Open Res Softw 4:1–6. https://doi.org/10.5334/jors.119

Jedlovec GJ, Nair U, Haines SL (2006) Detection of storm damage tracks with EOS data. Weather Forecast 21(3):249–267. https://doi.org/10.1175/WAF923.1

Katona B, Markowski P (2021) Assessing the influence of complex terrain on severe convective environments in northeastern Alabama. Weather Forecast 36:1003–1029. https://doi.org/10.1175/WAF-D-20-0136.1

Kirshbaum DJ, Adler B, Kalthoff N, Barthlott C, Serafin S (2018) Moist orographic convection: Physical mechanisms and links to surface-exchange processes. Atmosphere 9:80. https://doi.org/10.3390/atmos9030080

Kramar MR, Bluestein HB, Pazmany AL, Tuttle JD (2005) The Owl Horn radar signature in developing Southern Plains supercells. Mon Weather Rev 143(9):2608–2634. https://doi.org/10.1175/MWR2992.1

Lakshmanan V, Hondl K, Potvin CK, Preignitz D (2013) An improved method for estimating radar echo-top height. Weather Forecast 28(2):481–488. https://doi.org/10.1175/WAFD-12-00084.1

Lee BD, Jewett BF, Wilhelmson RB (2006) The 19 April 1996 Illinois tornado outbreak. Part II: Cell mergers and associated tornado incidence. Weather Forecast 21(4):449–464. https://doi.org/10.1175/WAF943.1

Lemon LR, Doswell CA III (1979) Severe thunderstorm evolution and mesocyclone structure as related to tornadogenesis. Mon Weather Rev 107(9):1184–1197. https://doi.org/10.1175/1520-0493(1979)107%3C1184:STEAMS%3E2.0.CO;2

Liu S, Kirshbaum DJ (2026) What makes boundary-layer convergence lines so effective at deep-convection initiation? J Atmos Sci 83:1111–1136. https://doi.org/10.1175/JAS-D-25-0081.1

Lopes MM, Nascimento EL (2024) Atmospheric environments associated with tornadoes in southern Brazil and neighboring areas as compared to other modes of convective hazards. Clim Dyn 62(5):3641–3667. https://doi.org/10.1007/s00382-023-07089-8

Lopes MM, Oliveira MI, Goede V, Ferreira V, Nascimento EL (2025) Damage Survey and Multisensor Analysis of a Cold Season Tornado Outbreak in Southern Brazil. J Appl Meteorol Climatol 64(7):831–855. https://doi.org/10.1175/JAMC-D-24-0146.1

Luz ESAM (2015) Estudo de casos de descargas atmosféricas utilizando espectroscopia sem fenda (SLITLESS). Dissertation, Instituto Nacional de Pesquisas Espaciais

Lyza AW, Flournoy MD (2023) The influence of cell mergers on supercell characteristics and tornado evolution on 27–28 April 2011. Mon Weather Rev 151(6):1551–1569. https://doi.org/10.1175/MWR-D-22-0189.1

Machado LAT, Lima WFA, Pinto O Jr, Morales CA (2009) Relationship between cloud-to-ground discharge and penetrative clouds: A multi-channel satellite application. Atmos Res 93(7):304–309. https://doi.org/10.1016/j.atmosres.2008.10.003

Mahalik MC, Smith BR, Elmore KL, Kingfield DM, Ortega KL, Smith TM (2019) Estimates of gradients in radar moments using a linear least squares derivative technique. Weather Forecast 34(2):415–434. https://doi.org/10.1175/WAF-D-18-0095.1

Miller ML, Lakshmanan V, Smith TM (2013) An automated method for depicting mesocyclone paths and intensities. Weather Forecast 28(3):570–585. https://doi.org/10.1175/WAF-D-12-00065.1

Murillo EM, Homeyer CR (2019) Severe hail fall and hailstorm detection using remote sensing observations. J Appl Meteorol Climatol 58(5):947–970. https://doi.org/10.1175/JAMC-D-18-0247.1

Nascimento EL, Held G, Gomes AM (2014) A multiple-vortex tornado in southeastern Brazil. Mon Weather Rev 142(9):3017–3037. https://doi.org/10.1175/MWR-D-13-00319.1

Nelson TC, Marquis J, Peters JM, Friedrich K (2022) Environmental controls on simulated deep moist convection initiation occurring during RELAMPAGO-CACTI. J Atmos Sci 79:1941–1964. https://doi.org/10.1175/JAS-D-21-0226.1

Nisi L, Hering A, Germann U, Martius O (2018) A 15-year hail streak climatology for the Alpine region. Q J R Meteorol Soc 144:1429–1449. https://doi.org/10.1002/qj.3286

Nixon CJ, Allen JT, Wilson MB, Bunkers MJ, Taszarek M (2024) Cell mergers, boundary interactions, and convective systems in cases of significant tornadoes and hail. Weather Forecast 39(10):1435–1458. https://doi.org/10.1175/WAF-D-23-0117.1

Oliveira MI, Puhales FS, Nascimento EL, Anabor V (2022) Integrated damage, visual, remote sensing, and environmental analysis of a strong tornado in southern Brazil. Atmos Res 274:106188. https://doi.org/10.1016/j.atmosres.2022.106188

Oliveira MI, Lopes MM, Goede V, Barreiro M, Salio P, Figueiredo EL, Xue M (2025) A multiscale analysis of the Dolores, Uruguay, tornadoes of 6 December 2012 and 15 April 2016. Atmos Res 316:107947. https://doi.org/10.1016/j.atmosres.2025.107947

Pardun TJ, Reinhart AE, Weiss CC, Rasmussen EE, Waugh SM, Houston AL (2026) The observed and Simulated Analysis of Supercellular Demise from 15 June 2019. Mon Weather Rev 154(2):311–330. https://doi.org/10.1175/MWR-D-25-0063.1

Piasecki K, Matczak P, Taszarek M, Czernecki B, Skop F, Sobisiak A (2023) Giant hail in Poland produced by a supercell merger in extreme instability – A sign of a warming climate? Atmos Res 292:106843. https://doi.org/10.1016/j.atmosres.2023.106843

Pinto O Jr, Naccarato KP, Saba MMF, Pinto IRCA, Abdo RF, Garcia SAM, Filho AC (2006) Recent upgrades to the Brazilian integrated lightning detection network. Proceedings of the ILDC, AZ, Amer. Meteor. Soc

Piscitelli FM, Ruiz JJ, Negri P, Salio P (2022) A multiyear radar-based climatology of supercell thunderstorms in central-eastern Argentina. Atmos Res 277:106283. https://doi.org/10.1016/j.atmosres.2022.106283

Ribeiro BZ, Bosart LF (2018) Elevated mixed layers and associated severe thunderstorm environments in South and North America. Mon Weather Rev 146(1):3–28. https://doi.org/10.1175/MWR-D-17-0121.1

Ribeiro BZ, Schild G, Santos L, Nascimento EL, Lopes MM, Goede V, dos Santos LO, Costa I, Ferreira V, Oliveira MI, Telles J, Furlan L (2022) The Brazilian severe storm reports database: methodology and a preliminary climatology. Preprints, 30th Conf. on Severe Local Storms, NM, Amer. Meteor. Soc

Rosa CE, Stefanello M, Facco DS, Roberti DR, Rossi FD, Nascimento EL, Degrazia GA (2022) Regional-scale meteorological characteristics of the Vento Norte phenomenon observed in Southern Brazil. Environ Fluid Mech 22(1):819–837. https://doi.org/10.1007/s10652-022-09855-4

Rotunno R, Klemp J (1985) On the Rotation and Propagation of Simulated Supercell Thunderstorms. J Atmos Sci 42(3):271–292. https://doi.org/10.1175/1520-0469(1985)042%3C0271:OTRAPO%3E2.0.CO;2

Sachidananda M, Zrinc DS (2000) Clutter filtering and spectral moment estimation for Doppler weather radars using staggered pulse repetition time (PRT). J Atmos Ocean Technol 17(3):323–331. https://doi.org/10.1175/1520-0426(2000)017%3C0323:CFASME%3E2.0.CO;2

Sachidananda M, Zrinc DS (2002) An improved clutter filtering and spectral moment estimation algorithm for staggered PRT sequences. J Atmos Ocean Technol 19(12):009–2019. https://doi.org/10.1175/1520-0426(2002)019%3C2009:AICFAS%3E2.0.CO;2

Saha S et al (2014) The NCEP climate forecast system version 2. J Clim 27(6):2185–2208. https://doi.org/10.1175/JCLI-D-12-00823.1

Salio P et al (2024) Toward a South American high-impact weather reports database. Bull Am Meteorol Soc 105(7):E1204–E1217. https://doi.org/10.1175/BAMS-D-23-0063.1

Schild G, Goede V, Lopes MM, Santos L, Ribeiro BZ, Oliveira M, dos Santos LO, Nascimento EL (2024) Environmental and Radar Analysis of a Long Track Tornado in Brazil. Preprints, 31st Conf. on Severe Local Storms, VA, Amer. Meteor. Soc

Schultz CJ, Petersen WA, Carey LD (2009) Preliminary development and evaluation of lightning jump algorithms for the real-time detection of severe weather. J Appl Meteorol Climatol 48(12):2543–2563. https://doi.org/10.1175/2009JAMC2237.1

Seluchi ME, Saulo AC, Nicolini M, Satyamurty P (2003) The northwestern Argentinean low: A study of two typical events. Mon Weather Rev 131(10):2361–2378. https://doi.org/10.1175/1520-0493(2003)131%3C2361:TNALAS%3E2.0.CO;2

Simpson J, Westcott NE, Clerman RJ, Pielke RA (1980) On cumulus mergers. Arch Meteor Geophys Bioklimatol A 29:1–40. https://doi.org/10.1007/BF02247731

Smith TM, Elmore KL (2004) The use of radial velocity derivatives to diagnose rotation and divergence. Preprints, 11th Conf. on Aviation, MA, Amer. Meteor. Soc

Soderholm B, Ronalds B, Kirshbaum DJ (2014) The evolution of convective storms initiated by an isolated mountain ridge. Mon Weather Rev 142:1430–1451. https://doi.org/10.1175/MWR-D-13-00280.1

Torres SM, Yannick F, Zrinc DS (2004) Design, implementation, and demonstration of a staggered PRT algorithm for the WSR-88D. J Atmos Ocean Technol 21(9):1389–1399. https://doi.org/10.1175/1520-0426(2004)021%3C1389:DIADOA%3E2.0.CO;2

van den Broeke MS, Wilson MB, van den Broeke CA, Healey DJ, Wood MJ, Nelson RE (2023) Polarimetric radar observations of a long-lived supercell and associated tornadoes on 10–11 December 2021. Mon Weather Rev 148(8):2501–2520. https://doi.org/10.1175/MWR-D-22-0330.1

Virtanen P et al (2020) SciPy 1.0: Fundamental algorithms for scientific computing in Python. Nat Methods 17(3):261–272. https://doi.org/10.1038/s41592-019-0686-2

Westcott N (1984) A historical perspective on cloud mergers. Bull Am Meteorol Soc 65(3):219–226. https://doi.org/10.1175/1520-0477(1984)065%3C0219:AHPOCM%3E2.0.CO;2

Westcott NE (1994) Merging of convective clouds: Cloud initiation, bridging, and subsequent growth. Mon Weather Rev 122:780–790. https://doi.org/10.1175/1520-0493(1994)122%3C0780:MOCCCI%3E2.0.CO;2

Witt A, Eilts MD, Stumpf GJ, Johnson JT, Mitchell EDW, Thomas KW (1998) An enhanced hail detection algorithm for the WSR-88D. Weather Forecast 13(2):286–303. https://doi.org/10.1175/1520-0434(1998)013%3C0286:AEHDAF%3E2.0.CO;2

Wurman J, Richardson Y, Alexander C, Weygandt S, Zhang PF (2007) Dual-Doppler and single-Doppler analysis of a tornadic storm undergoing mergers and repeated tornadogenesis. Mon Weather Rev 135:736–758. https://doi.org/10.1175/MWR3276.1

Zrinc DS, Mahapatra P (1985) Two methods of ambiguity resolution in pulse Doppler weather radars. IEEE Trans Aerosp Electron Syst AES –21(4):470–483. https://doi.org/10.1109/TAES.1985.310635